Waste Management Bulletin 4 (2026) 100281

Contents lists available at ScienceDirect

Waste Management Bulletin

journal homepage: www.elsevier.com/locate/wmb

Study of the phase composition (Zn, ZnO) of anodes recovered from spent alkaline batteries, with respect to their residual voltage

Juan Carlos Rodriguez Lopez [a], Enrique Vigueras Santiago [b], N. García-González [c], V.H. Castrejón-Sánchez [c], Marco Camacho-López [b], Susana Hernández López [b,*]

[a] Universidad Autónoma del Estado de México (UAEMEX), Programa de Maestría en Ciencia de Materiales, Facultad de Química, Campus Rosedal Km 14.5 Carretera Toluca-Atlacomulco, Toluca C.P 50200, Mexico

[b] Universidad Autónoma del Estado de México (UAEMEX), Laboratorio de Investigación y Desarrollo de Materiales Avanzados (LIDMA), Facultad de Química, Campus Rosedal Km 14.5 Carretera Toluca-Atlacomulco, Toluca C.P 50200, Mexico

[c] Tecnológico de Estudios Superiores de Jocotitlán, Departamento de Ingeniería Química e Ingeniería de Materiales, Carretera Toluca-Atlacomulco km 44.8, Ejido de San Juan y San Agustín, Jocotitlán, Edo. México C.P. 50700, Mexico

ARTICLE INFO

Keywords:
Anodes
Spent batteries
Zn
ZnO
Residual voltage

ABSTRACT

The development of advanced materials with tailored properties has long been a cornerstone of technological innovation. Increasingly, attention is shifting toward the transformation of end-of-life waste into valuable resources. Spent alkaline batteries, when improperly disposed of as electronic waste (e-waste), pose significant environmental hazards due to their content of toxic metals, which can leach into soil and groundwater. These metals may also undergo physicochemical transformations through interactions with other waste materials. This study investigates the anode recovered from spent alkaline batteries discharged to varying residual voltages. The recovery process involved manual separation, followed by washing with deionized water, filtration, and drying at 50 °C for 48 h prior to characterization. The resulting particles exhibited photoluminescent properties that correlated with the residual voltage of the batteries. Structural analysis revealed the coexistence of Zinc and Zinc Oxide (Zn/ZnO) phases at voltages above 0.78 V, while only ZnO was present below this threshold. The ZnO content was found to depend on the degree of battery depletion, with the residual voltage directly influencing the Zn/ZnO phase ratio.

Introduction

Zinc oxide (ZnO) is a semiconductor that continues to attract significant research interest due to its expanding range of applications in optoelectronic devices, sensors, solar cells, photocatalysis, biomedicine, and self-cleaning surfaces. Its appeal lies in its chemical stability and unique optical and electrical properties (Al-luhaibi and Sendi, 2022; Gulab et al., 2024; Kumar et al., 2013; Liu et al., 2013; Nguyen et al., 2020). ZnO is widely used across various industries. In cosmetics and pharmaceuticals, it serves as a key ingredient in sunscreens, makeup, antibacterial treatments, dietary supplements, and as an excipient in tablet formulations (Gulab et al., 2024). It is also found in certain vaccines and medications, including insulin (Kumar et al., 2013). In the medical field, ZnO's antimicrobial properties and biocompatibility make it suitable for wound dressings, dental cements, and other biomedical applications (Liu et al., 2013).

Due to its semiconductor characteristics, particularly its band gap of approximately 3.3 eV, ZnO is extensively used in the electronics industry for the fabrication of transistors, diodes, and sensors (Noman et al., 2022). In the paint industry, it functions as a white pigment that enhances the brightness of paper, plastics, and coatings while maintaining mechanical properties such as flexibility and rigidity. ZnO also acts as a catalyst in chemical processes like the transesterification of vegetable oils and wastewater treatment. In nanotechnology, ZnO is of particular interest due to its tunable properties at the nanoscale; when combined with metallic nanoparticles, its catalytic performance is significantly enhanced (Kumar et al., 2013).

Although ZnO can be synthesized through various chemical and

* Corresponding author.
E-mail addresses: juancarlos863@live.com (J.C. Rodriguez Lopez), evigueras@uaemex.mx (E. Vigueras Santiago), nidia.gonzalez@tesjo.edu.mx (N. García-González), victor.castrejon@tesjo.edu.mx (V.H. Castrejón-Sánchez), macamacholo@uaemex.mx (M. Camacho-López), shernandezl@uaemex.mx (S. Hernández López).

https://doi.org/10.1016/j.wmb.2026.100281

Available online 22 January 2026

physical methods to achieve specific morphologies, one form remains relatively understudied: ZnO recovered from the anodes of spent alkaline batteries (Cebriano et al., 2017; Deep et al., 2011). This oxide is a byproduct of the electrochemical reactions that occur during battery discharge. Recovering and reusing ZnO from spent batteries could contribute to the development of sustainable materials and open new avenues for secondary applications (Lopez et al., 2023; Lorero et al., 2022). Several research groups have already characterized the physicochemical properties of ZnO derived from discarded batteries (Cebriano et al., 2017; Deep et al., 2011).

Battery waste is a growing concern. In Mexico alone, approximately 780 million batteries are discarded annually, most of which are non-rechargeable alkaline types (Milenio®, 2023). Per capita consumption has increased dramatically, from about 5 batteries per person in the 1990 s to over 12 today, driven by the proliferation of portable electronic devices. Globally, the alkaline battery market was valued at USD 8.7 billion in 2024 and is projected to grow at a compound annual rate of 5.2% through 2034 (Global Market Insights, 2024). Alkaline batteries dominate the primary (non-rechargeable) battery segment, with billions sold annually for use in household electronics such as remote controls, flashlights, toys, and radios. Despite their ubiquity, less than 10% of alkaline batteries are properly recycled worldwide. In many countries—including Mexico—they end up in landfills, posing environmental risks due to residual heavy metals and electrolytes.

Current recovery methods for alkaline battery components—particularly zinc from the anode and manganese dioxide from the cathode—are typically energy-intensive and generate chemical residues. Chemical processes (Toro et al., 2023; Bae et al., 2025) rely on acidic or alkaline leaching using solutions such as sulfuric acid or sodium hydroxide to dissolve the metals. Zinc is recovered as zinc sulfate or metallic zinc, while manganese is precipitated as manganese dioxide (MnO_2). Thermal processes involve heating battery materials to high temperatures (800–1000 °C) to volatilize zinc and separate it from other components (Jain et al., 2023). Although effective at scale, these methods consume significant energy and produce greenhouse gases and toxic byproducts, making them less environmentally favorable.

Liquid–liquid extraction is recognized as a convenient and cost-effective method that requires relatively short operational times. Numerous extractants have been investigated for the removal and separation of Zn(II) from spent batteries, with recent attention focused on ionic liquids. Mandeep (Mandeep et al., 2019) reported the synthesis of ZnO from Zn–C battery leach liquor using Cyphos IL 102 as the extractant, yielding a Zn-enriched organic phase. This phase was subsequently treated to precipitate zinc compounds, which upon thermal decomposition produced ZnO nanoparticles. The resulting ZnO was employed as a photocatalyst for the degradation of methyl orange dye, underscoring its potential in environmental remediation. Nevertheless, chemical reagents were required for both the separation process and the synthesis of ZnO.

In a related study (Stefan et al., 2024), Mn-doped ZnO particles were synthesized by annealing the anodic paste collected from fully discharged Zn–MnO_2 alkaline batteries (Energizer) at different temperatures. The doping effect was achieved by exploiting the partial contamination of electrodes after discharge. Once separated, the anodic paste was treated with a water–alcohol mixture (1:1 v/v) to remove soluble impurities, followed by neutralization with hydrochloric acid (3 M). The authors demonstrated the functional properties and applications of the resulting materials, including photocatalytic activity under visible light irradiation for the degradation of Rhodamine B and oxytetracycline. Furthermore, they fabricated symmetric supercapacitors and evaluated their energy storage performance using various electrochemical techniques.

In 2021 (Sunaina et al., 2021), an eco-friendly approach was reported for the recovery and utilization of zinc oxide (ZnO) nanostructures from spent Zn–Mn alkaline batteries. ZnO separation was achieved for the first time by simply washing the anodic component with distilled water, exploiting the basicity of the medium to dissolve impurities and yield pure ZnO rods. The recovered ZnO rods exhibited promising field emission properties, highlighting their potential application in advanced electronic devices while simultaneously addressing hazardous battery waste management.

The present study adopts the same green and straightforward method as (Sunaina et al., 2021) for recovering anode components—typically a mixture of Zn and ZnO phases—from spent AA Duracell alkaline batteries collected from our laboratory's recycling center. One of the objectives is to determine the discharge limit at which only the ZnO phase remains, to characterize it without further modification. It should be noted that batteries recovered from landfills may exhibit compromised purity (Bae et al., 2025), which can affect the reproducibility of their properties. In this study, the recovered ZnO displayed microrod morphology and photoluminescent properties that varied with the residual voltage—a parameter directly linked to the Zn/ZnO composition.

Duracell alkaline batteries follow a non-linear discharge curve, starting at 1.5 V and gradually dropping to ~ 0.9 V before becoming ineffective (REDWAY, 2024). At this stage, zinc has not been fully converted into ZnO, meaning that batteries discarded at different voltages contain varying Zn/ZnO ratios. These variations are attributed to the electrochemical discharge mechanism (Sunaina et al., 2021; Collins et al., 2018; Horna and Shao-Horn, 2003; Durena and Zukuls, 2023) in which metallic zinc is progressively oxidized to zinc oxide in an alkaline medium, as explained as follow: The anode component of the alkaline Zn-MnO_2 batteries is constituted of mixture of metallic Zn and potassium hydroxide (KOH), which acts as the electrolyte. The observed Zn/ZnO ratio variations are a direct consequence of the discharge pathway, where zinc metal is progressively converted into ZnO under alkaline conditions in a sequential transformation: **metallic Zn → soluble zincate → ZnO precipitation → passivation → heterogeneous consumption**. The overall reaction at the anode can be expressed as Eq. (1):

$$Zn_{(s)} + 2(OH)^- \rightarrow ZnO_{(s)} + H_2O + 2e^- \quad (1)$$

This process provides the electrons that flow through the external circuit toward the cathode, where manganese dioxide (MnO_2) undergoes reduction.

Stepwise mechanism

1. **Initial oxidation and complex formation.** Metallic zinc undergoes anodic dissolution in the alkaline medium. The first step involves the formation of soluble zincate species (**Eq. (2)**). The tetrahydroxozincate(II) ion is the predominant soluble species under strongly alkaline conditions

$$Zn_{(s)} + 4(OH)^- \rightarrow Zn(OH)_4^{2-} + 2e^- \quad (2)$$

2. **Precipitation of zinc oxide.** The zincate ion is metastable and tends to decompose, releasing hydroxide and precipitating zinc oxide (**Eq. (3)**). This precipitation leads to the progressive accumulation of ZnO on the surface of the zinc particles

$$Zn(OH)_4^{2-} \rightarrow ZnO + H_2O + 2(OH)^- \quad (3)$$

3. **Passivation Layer formation.** The ZnO formed is poorly conductive and adheres to the zinc surface, creating a passivation layer. This layer impedes the transport of hydroxide ions to the underlying metallic zinc, thereby slowing further oxidation. The thickness and morphology of this layer strongly influence the effective utilization of zinc and the Zn/ZnO ratio observed in spent anodes
4. **Heterogeneous consumption of zinc.** Due to differences in particle size, porosity, and electrical connectivity within the zinc anode matrix, the oxidation process is spatially heterogeneous. Regions

with better electronic contact and higher local current density oxidize more rapidly, while poorly connected zones retain metallic zinc even at advanced states of discharge. This heterogeneity explains the variability in Zn/ZnO proportions extracted from used alkaline cells

The final Zn/ZnO proportion is governed by the state of discharge, current distribution, and secondary processes such as passivation, dissolution, and reprecipitation, all of which modulate the kinetics and spatial uniformity of zinc utilization (Durena and Zukuls, 2023). However, despite the complex internal processes occurring during battery operation, as well as the external conditions to which the cells are subjected during use, it is particularly relevant to identify whether a voltage threshold exists at which the complete transformation of Zn into ZnO takes place.

The recovery method proposed in this work is environmentally friendly, requiring neither energy input nor chemical reagents. Structural characterization confirmed that the recovered ZnO possesses high purity, and its optical properties can be tuned according to the level of battery discharge.

Materials and methods

Materials

A total of 32 alkaline batteries (MnO_2–Zn), model LR6, Duracell®, were collected from the collection center of the Advanced Materials Research Laboratory (LIDMA), UAEMEX. Zinc powder (Commercial purified water (ePura®) and deionized water were used without any additional treatment.

Methods

Differential scanning calorimetry (DSC)

Analyses were performed using a PerkinElmer simultaneous thermal analyzer (STA 8000) within a temperature range of 300 – 500 °C, employing a heating rate of 20 °C/min and a nitrogen flow rate of 20 mL/min.

X-ray diffraction (XRD)

Measurements were conducted on a Bruker D8 DISCOVER diffractometer using CuKα radiation (λ = 1.54 Å). Operating conditions were 30 kV and 30 mA, with a 2θ scan range from 10° to 80°, a step size of 0.15°, and a measurement time of 1 s per step.

Scanning electron microscopy and energy dispersive spectroscopy (SEM-EDS)

Morphological and elemental analyses were performed using a JEOL JSM-IT100 scanning electron microscope, equipped with an X-ray microprobe for elemental detection. The acceleration voltage was 20 kV in secondary electron mode, with a working distance of 11 mm. Micrographs were obtained at 10000x magnifications. Prior to analysis, samples were coated with gold using an Auto Agar sputter coater (model 108A). A gold target of 99.995% purity was used, and all samples were coated for 30 s.

Raman spectroscopy

Raman spectra were obtained using a HORIBA XploRA PLUS spectrophotometer, with a 532 nm laser excitation source operating at 10% power. The acquisition time was 10 s, with 60 accumulations, covering a spectral range of 200–800 cm^{-1}.

Photoluminescence (PL)

Photoluminescence spectra were recorded using a STELLARNET fiber-optic UV–Vis spectrophotometer, with sample excitation provided by a DARKDAWN UV lamp at a wavelength of 365 nm.

Thermal oxidation

A sample of zinc oxide (ZnO) was synthesized via thermal oxidation of metallic zinc (99.995% purity) at 900 °C for 9 h under atmospheric conditions, using a Carbolite tubular furnace.

Experimental methodology

This section outlines the methodology employed for the collection and purification of particles containing a Zn/ZnO mixture, separated from the anodes of spent LR6-type alkaline batteries. Ther residual voltage of 32 batteries was measured using a digital multimeter. Based on the measurements, the batteries were classified into groups according to their average residual voltage: 1.5, ~1.3, ~1.2, ~1.0, ~0.92, ~0.78, ~0.27, and ~ 0.03 V. Four batteries were analyzed in each group, and the statistical variation of residual voltages was assessed, confirming that the batteries within each group exhibited consistent values (**Table S1** of supplementary material). Following classification, each battery was disassembled, thoroughly cleaned, and the separated powders were combined for subsequent characterization. The recovered particle mixture exhibited a whitish-gray color, with slight variations depending on its specific composition

To recover the whitish-gray mass from the anode, the following procedure was employed: the plastic casing was removed using wire cutters. The metal casing was then detached by making two cuts—one longitudinal along the battery axis and one transverse at the negative pole—using a clamp-on vise to secure the battery and a hacksaw to perform the cuts. Once the casing was opened, the internal components were separated using dissecting forceps. The membrane enclosing the anode was carefully removed to avoid contamination of the target particles.

The collected anode material was subjected to sequential washing to remove residual KOH electrolyte. The material was placed in a 1 L beaker containing 800 mL of purified water and stirred magnetically for 1 h. The resulting suspension was filtered using an aluminum strainer. This washing and filtration process was repeated three additional times: the first two washes were performed with purified water, and the third with deionized water. This treatment effectively reduced the pH from 14 to neutral (pH 7). The wet whitish-gray mass obtained from each anode was weighed and dried in an oven at 50 °C until a constant weight was achieved (approximately 48 h). On average, 1.2 ± 0.5 g of dry powder was obtained per anode. The resulting powder was characterized using Differential Scanning Calorimetry (DSC), X-ray Diffraction (XRD), Scanning Electron Microscopy coupled with Energy Dispersive Spectroscopy (SEM-EDS), Raman Spectroscopy, and Photoluminescence (PL).

Fig. 1 illustrates the general flow diagram of the recovery and washing process for whitish-gray particles containing both ZnO and Zn phases, separated of the anode from LR6-type alkaline batteries.

Results

Differential Scanning Calorimetry (DSC)

Differential Scanning Calorimetry (DSC) was employed to determine the minimum residual voltage at which only the ZnO phase remains in the recovered material from spent alkaline batteries. The analysis focused on the endothermic peak corresponding to the melting point of metallic zinc, typically observed around 420 °C. Fig. 2 presents the calorimetric curves corresponding to particles recovered from the anodes of spent alkaline batteries with varying residual voltages. A maximum in the enthalpic curve was observed at approximately 420 °C, consistent with the melting temperature of metallic Zn as reported in the literature (Bantikatla et al., 2019; Noohi et al., 2022). This peak, clearly visible in samples from new batteries (1.5 V), gradually diminished as the residual voltage decreased (e.g., 0.92 V). At an average residual voltage of 0.78 V or lower, the endothermic signal was no longer

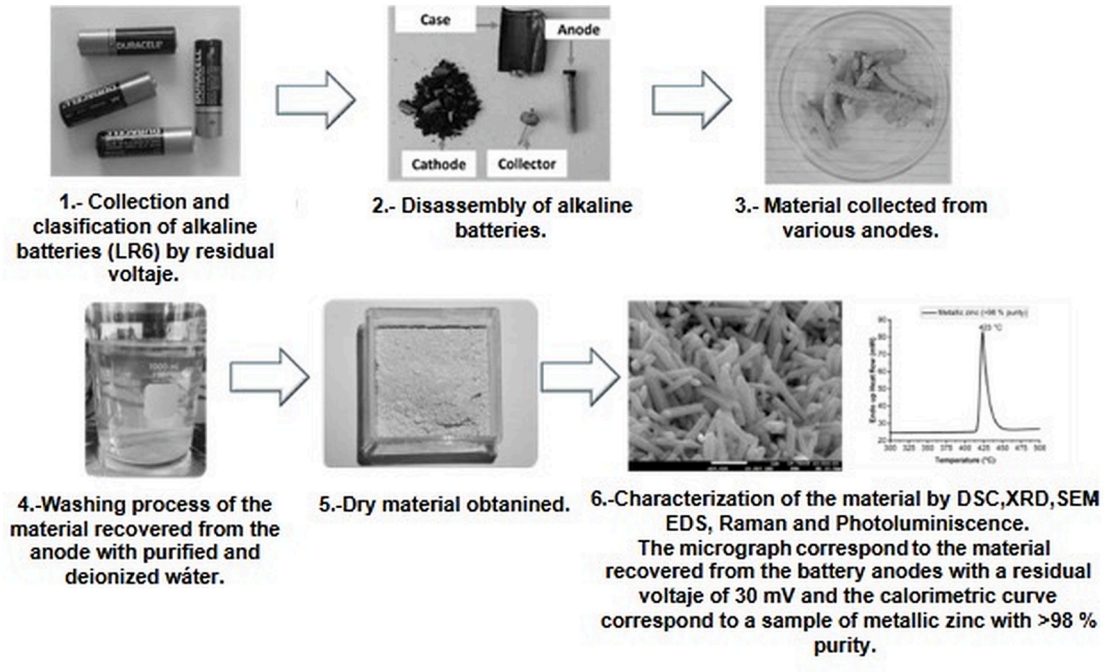

Fig. 1. General process of recovery and washing of Zn/ZnO particles from alkaline batteries type LR6 [Authors].

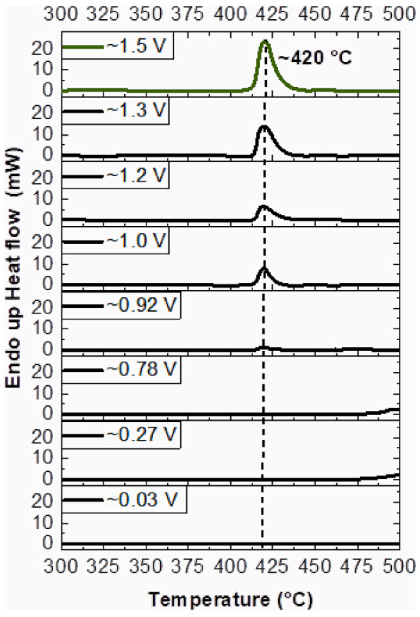

Fig. 2. DSC endothermic curves of the ZnO/Zn particles obtained from anodes recovered from spent alkaline batteries with different residual voltage [Authors].

present, indicating the absence of metallic Zn and confirming that only ZnO remained in the recovered material.

X-ray diffraction (XRD)

X-ray diffraction analysis was conducted to identify the crystalline phases present in the recovered particles and to corroborate the DSC findings. Diffractograms of a standard metallic zinc sample (99.995% purity) and particles recovered from new alkaline batteries (1.5 V residual voltage) revealed seven diffraction peaks at 2θ values of 36.10, 38.80, 43.00, 54.10, 69.85, 70.45, and 76.90°, and 36.40, 39.10, 43.30, 54.40, 70.15, 70.90, and 77.05°, respectively. These peaks correspond to the crystallographic planes (002), (100), (101), (102), (103), (110), and (004) of metallic Zn, as indexed by JCPDS card No. 00–004-0831. The slight shifts in 2θ values between the reference and recovered samples may be attributed to the lattice strain of ZnO, probably associated with structural defects during the electrochemical reaction of alkaline batteries. Furthermore, they should be interpreted considering instrumental variations. Importantly, no additional peaks were observed, indicating the absence of contaminants or residuals from the recovery process.

Fig. 3 shows the XRD patterns of Zn/ZnO mixtures recovered from ASAB samples with residual voltages of 1.3, 1.2, 1.0, and 0.92 V. These diffractograms exhibit overlapping peaks from both Zn and ZnO phases. Peaks corresponding to metallic Zn (JCPDS 00–004-0831) are marked with an asterisk (*), while those associated with ZnO (JCPDS 00–036-1451) are denoted with a bullet (•). For clarity, the abbreviation "ASAB" will be used throughout the text to refer to "anode recovered from spent alkaline batteries".

Fig. 4 (4a) shows ZnO_{ref} obtained by thermal oxidation of metallic zinc (99.995% purity) at 900 °C for 9 h. For clarity, the ZnO_{ref} obtained by thermal oxidation of metallic Zn was used solely as a reference standard, together with metallic Zn of equivalent purity. These comparative samples serve only to support phase identification in Zn/ZnO mixtures and are not part of the recovered material under discussion. The three remaining figures display the XRD patterns of ZnO recovered from ASAB with average residual voltages of 0.78 (4b), 0.27 (4c), and 0.03 V (4d). All four samples exhibited the characteristic hexagonal wurtzite structure of ZnO. Eleven distinct diffraction peaks were identified at 2θ values of 31.75, 34.45, 36.25, 47.50, 56.60, 62.80, 66.40, 67.90, 69.10, 72.55, and 76.90°, corresponding to the crystallographic planes (100), (002), (101), (102), (110), (103), (200), (112), (201), (004), and (202), in agreement with JCPDS card No. 00–036-1451.

Notably, no diffraction signals associated with metallic Zn were detected in these samples, confirming complete oxidation of the precursor material. Structural parameters including lattice constants *a* and *c*, unit cell volume, average crystallite size, dislocation density, and microstrain were calculated based on the diffraction data (Kahouli et al.,

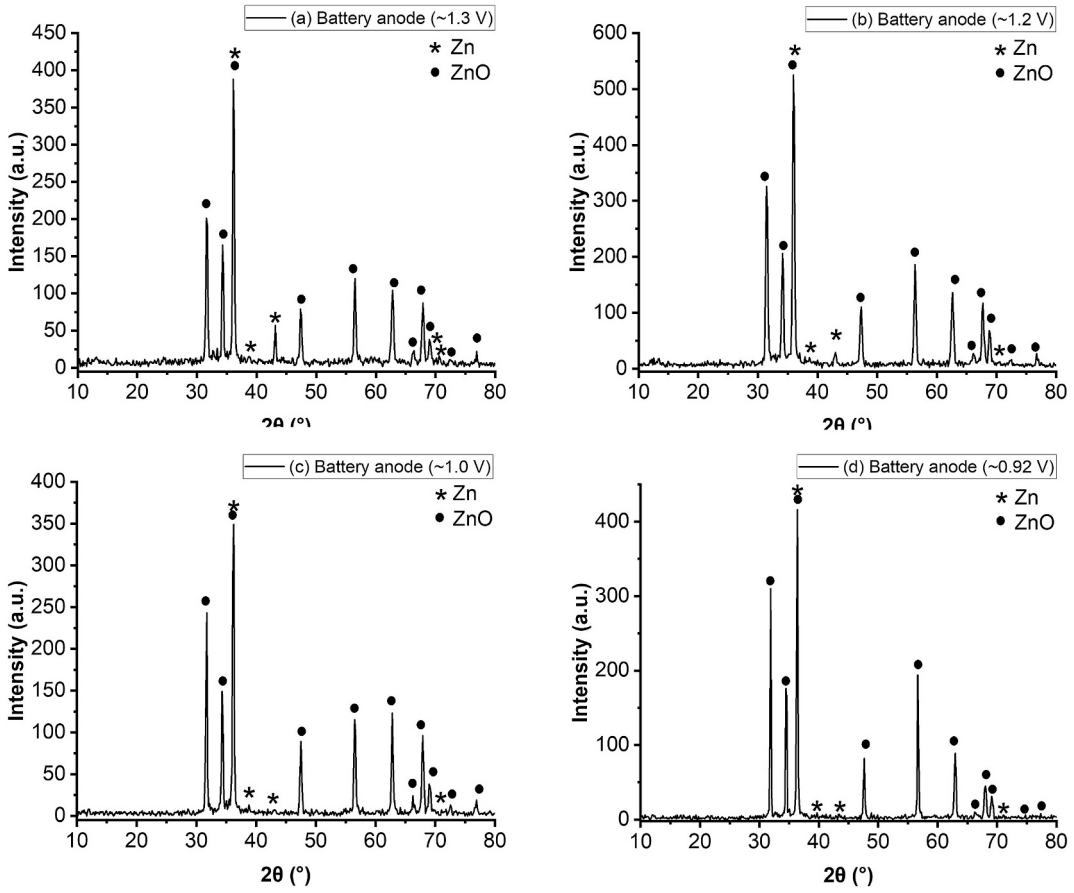

Fig. 3. Diffractograms of the Zn/ZnO particles obtained from ASAB with different residual voltage [Authors].

2015; Raoufi, 2013a). Table 1 summarizes the results for the structural parameters—crystallite size, dislocation density, and microstrain—determined by X-ray diffraction, together with their statistical variation.

X-ray diffraction analyses corroborated the findings obtained from DSC. Particles recovered from ASAB with a residual voltage of 1.5 V corresponded exclusively to the metallic Zn phase. In contrast, samples from batteries with residual voltages in the range of 1.3 – 0.92 V exhibited a mixture of Zn and ZnO phases. Below 0.78 V, only ZnO was detected, indicating complete oxidation of the zinc content. As observed, the crystallite size (D) of ZnO decreases with decreasing residual voltage, suggesting that battery degradation leads to greater fragmentation or refinement of the crystallites. This reduction in size is accompanied by an increase in dislocation density, which may indicate that the degradation process introduces internal defects and residual stresses within the ZnO material. Moreover, the unit cell volume (V) was found to be slightly higher in ZnO extracted from batteries with lower remaining voltage (~48.22 $Å^3$ at 30 mV). Both dislocation density and microstrain also increased as the residual voltage decreased. These findings suggest that the remaining voltage in spent batteries has a direct influence on the microstructural characteristics of the recovered ZnO, likely due to variations in the electrochemical environment during discharge; in addition, the speed and mode of discharge can influence of these structural parameters of ZnO.

All samples exhibited a pronounced statistical variation in crystallite size, reflecting a heterogeneous microstructural distribution consistent with the broadening observed in polycrystalline diffraction peaks. Similarly, dislocation density showed considerable variability; however, the sample at approximately 0.27 V-SABA displayed a markedly lower variation (1.7), suggesting a possible microstructural "maturation," that is, a more advanced stage of transformation into ZnO. This stage may have homogenized the dislocation network, thereby reducing its variability and providing partial stress relief along with a more uniform redistribution of dislocations compared to the other samples. In contrast, the pronounced microstrain anisotropy observed at ~ 0.78 V-SABA, even when only ZnO was detected, cannot be attributed to phase coexistence. At this stage, the anisotropy is instead governed by crystallographic orientation and defect incorporation within ZnO itself, accounting for the maximum variation observed among the residual voltage groups.

The relative proportion of metallic (Zn) and oxide (ZnO) phases in the discharged anodes was determined by Rietveld refinement following (Dhingra et al., 2018) (**Fig. S5** of Supplementary material), using the atomic positions and occupancies reported for Zn and ZnO (**Table S3** of Supplementary material). The estimated Zn/ZnO ratios at different residual voltages were as follows: **1.5 V (100/0), 1.3 V (5.7/94.3), 1.2 V (4/96), 1.0 V (1.2/98.8), and 0.92 V (1.6/98.4)**. When analyzed as a function of residual voltage, these results reveal a sharp transition between 1.5 V, where the material is entirely metallic (100% Zn), and 1.3 V, where ZnO already accounts for 94.3% of the crystalline phase. Below 1.2 V, the metallic Zn fraction becomes negligible, with the anode consisting of more than 95% ZnO.

The variations in Zn/ZnO proportions can be attributed to several interrelated factors. First, the degree of battery discharge plays a decisive role: partially used cells retain a higher fraction of metallic Zn, whereas fully exhausted cells exhibit a predominance of ZnO. Second, the distribution of current density and the microstructural heterogeneity of the anode lead to uneven oxidation of zinc across the electrode surface. In addition, secondary phenomena contribute to the observed ratios, including the transient formation of zinc hydroxide intermediates ($Zn(OH)_2$) and the partial dissolution of Zn^{2+} ions into the electrolyte, followed by their reprecipitation as ZnO. Operating conditions such as

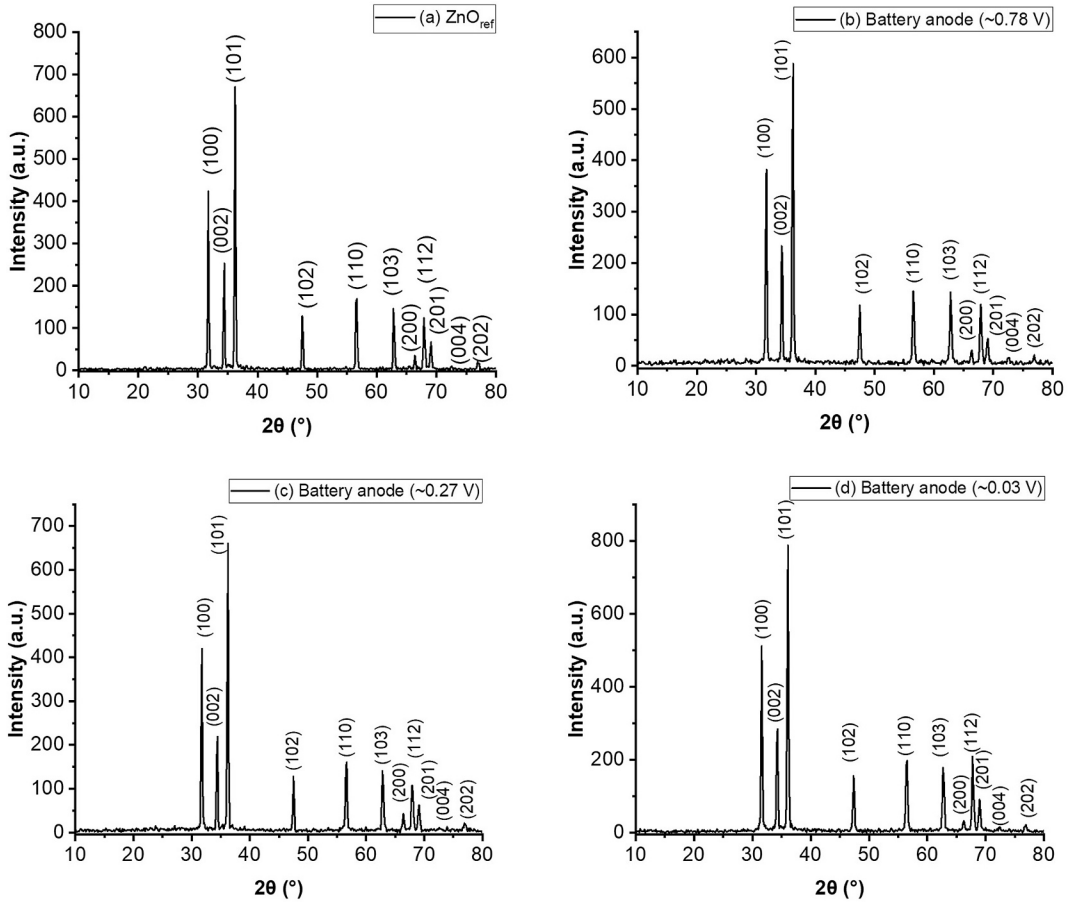

Fig. 4. Diffractograms of (a) ZnO_{ref}, and of the particles recovered from 0.78 V (a), 0.27 V (b) and 0.03 V (d)- ASAB [Authors].

Table 1
Structural parameters of Zn, ZnO obtained by oxidation and recovered from ASAB [Authors].

Sample	Structural parameters						
	a (Å)	**c (Å)**	**c/a**	**V (Å^3)**	**D (nm)**	**Dislocation Density δ x 10^{-4} (nm^{-2})**	**Microstress ε x 10^{-4}**
JCPDS 00–004-0831 Zn	**2.665**	**4.947**	**1.8562**	**30.43**	–	–	–
Zinc 99.995%	2.67	4.97	1.85	30.83	46.8	6.67	19.7
~1.5 V – ASAB	2.65	4.93	1.85	30.14	55.7 ± 26.7	4.9 ± 3.1	16.8 ± 5.8
JCPDS 00–036-1451 ZnO	**3.249**	**5.206**	**1.602**	**47.62**	–	–	–
ZnO_{ref}	3.25	5.20	1.59	47.58	41.8 ± 20.5	8.1 ± 4	22.5 ± 9.1
~0.78 V- ASAB	3.25	5.22	1.60	47.78	39.2 ± 17.2	9.4 ± 5.4	24.1 ± 11.5
~0.27 V- ASAB	3.25	5.20	1.59	47.58	37 ± 16.6	10.3 ± 1.7	24.5 ± 9.1
~0.03 V- ASAB	3.26	5.22	1.59	48.22	38.4 ± 17.7	10.3 ± 6.1	25.1 ± 12.5

temperature, humidity, and discharge cycling further influence the kinetics of zinc oxidation. Finally, recycling and extraction methods can alter the measured Zn/ZnO proportion, since soluble Zn^{2+} species may be lost or converted into ZnO during leaching or separation processes.

As an example of the variability introduced by these factors, (Sunaina et al., 2021) reported a controlled discharge experiment starting at 1.6 V with a fresh battery composed of metallic Zn (~56%) and ZnO (~44%). Over 15 days of operation, the composition evolved to predominantly ZnO (~92%), with the cell voltage decreasing to 0.67 V, which was considered fully discharged. In contrast, our study (based on XRD) revealed no detectable ZnO in a new battery, and at 0.78 V—still above the 0.67 V threshold—we observed, by DSC and XRD, no residual Zn phase, whereas the referenced work reported ~ 8% metallic Zn remaining at that stage.

Scanning Electron Microscopy (SEM)

Fig. 5a presents SEM micrographs of grayish particles recovered from the anodes of 1.5 V alkaline batteries. Based on the corresponding XRD pattern, these particles were identified as metallic zinc. The observed morphologies were predominantly irregular tetrahedral structures, with particle sizes varying across the sample and an average diameter of approximately 1.96 μm.

Fig. 5b through 6e display SEM micrographs of particles recovered from ASAB with residual voltages of 1.3 V, 0.92 V, 0.27 V and 0.30 V, respectively. All images were captured at a magnification of 10,000x to enable direct comparison of particle morphology and size across different voltage levels. In general, particles recovered from the anodes of LR6-type alkaline battery with residual voltages ranging from 1.3 V to 0.03 V appeared as agglomerates of bars with irregular hexagonal cross-sections and rough surfaces. These bars exhibited non-uniform

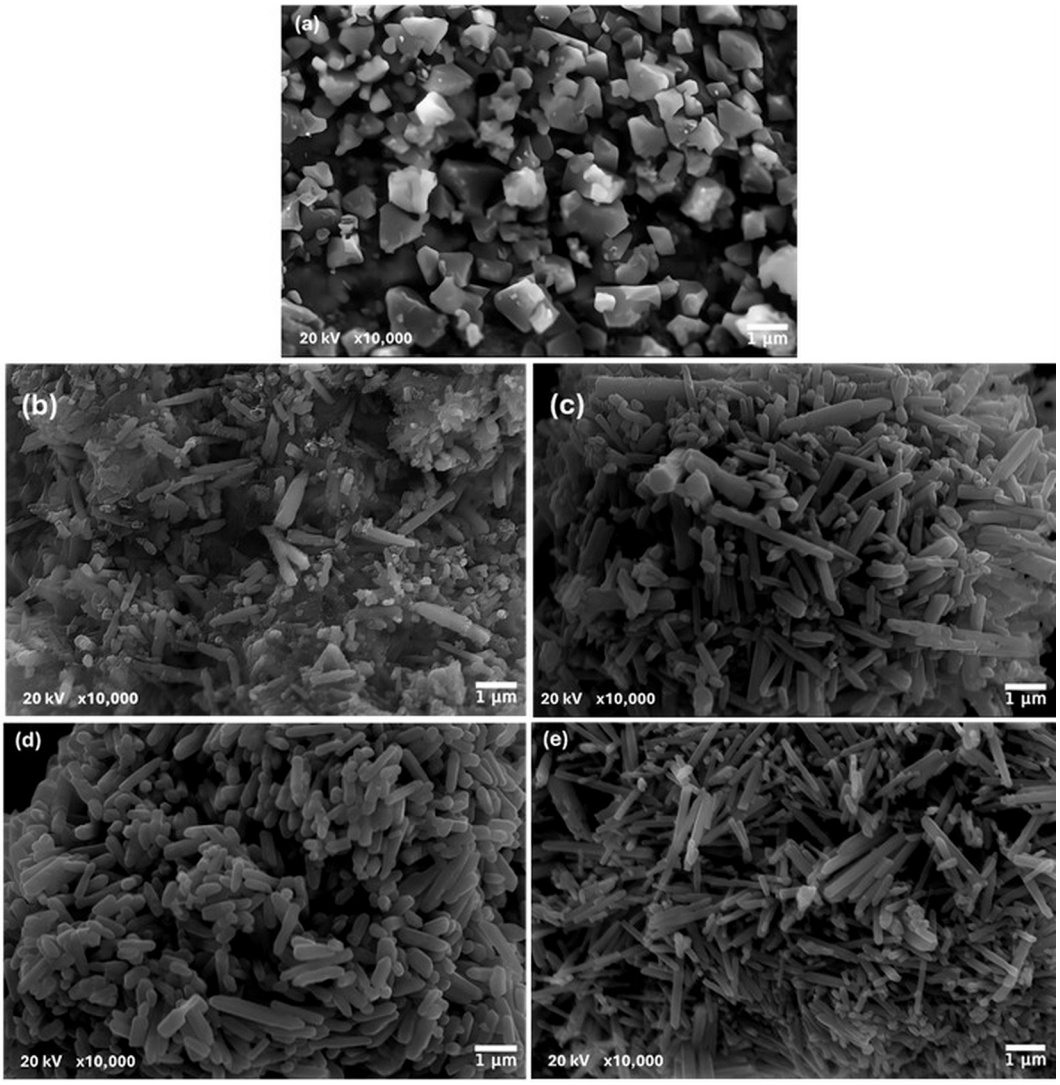

Fig. 5. Micrographs at 10000x amplifications of (a) anodes of 1.5 V alkaline batteries, and. particles recovered from (b) ~ 1.3 V-ASAB, (c) ~ 0.92 V-ASAB, (d) 0.27-ASAB V and (e) 0.03 V-ASAB [Authors].

profiles, with central regions appearing wider than the ends, suggesting anisotropic growth behavior.

The average lengths and diameters of these structures are summarized in Table 2, along with their corresponding aspect ratios ($\alpha = L/d$). Notably, the aspect ratio increased as the residual voltage decreased, indicating a voltage-dependent morphological evolution of the recovered particles. This trend suggests that lower residual voltages may promote elongation or directional growth, likely due to variations in the electrochemical environment, localized dissolution dynamics, the rate and mode of discharge.

This rod-like morphology is consistent with that reported in (Sunaina et al., 2021), where the authors observed the formation of flower-like structures at intermediate discharge stages, which subsequently evolved into well-defined ZnO nanorods with average dimensions of 1.5–2.0 µm in length and 0.8 µm in diameter. In contrast, in our study no intermediate morphologies were detected, and smaller rod diameters were detected, with the minimum value reaching 0.2 µm at residual voltages below 1.0 V.

Table 2
Aspect ratio of particles recovered from ASAB at different residual voltages [Authors].

Residual voltages (V)	Length, L (µM)	Average diameter (d) (µm)	Aspect ratio (α)
1.3	1.44	1.28	5.0
1.2	3.38	0.78	4.6
1.0	1.84	0.46	4.0
0.92	1.52	0.33	4.5
0.78	1.13	0.20	5.4
0.27	1.51	0.28	5.3
0.03	2.75	0.36	7.6

Raman spectroscopy

According to group theory, the hexagonal wurtzite structure of ZnO exhibits Raman-active optical phonon modes with symmetries $A_1 + 2E_2 + E_1$. The nonpolar E_2 mode appears at two distinct frequencies: E_2 (low), associated with vibrations of the Zn sublattice, and E_2 (high), linked to oxygen atoms. In contrast, the polar A_1 and E_1 modes split into transverse optical (TO) and longitudinal optical (LO) components due to their interaction with the macroscopic electric field (de Sousa e Silva and Franco, 2020; Xue et al., 2014).

Fig. 6 shows the Raman spectrum of ZnO_{ref} (only to support identification) revealing five vibrational modes: E_2 (low), A_1 (TO), E_1 (TO), E_2 (high), and E_1 (LO), located at 334, 380, 408, 438, and 584 cm^{-1},

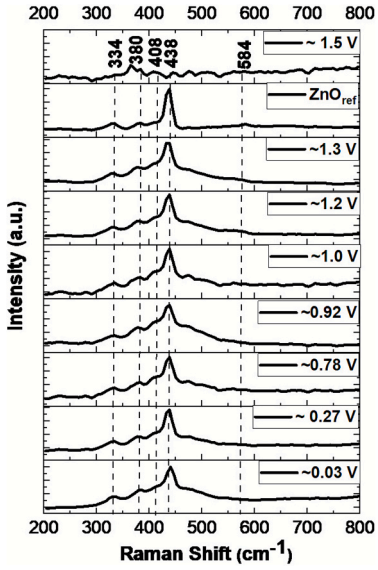

Fig. 6. Raman spectra of particles obtained from ASAB with different residual voltage [Authors].

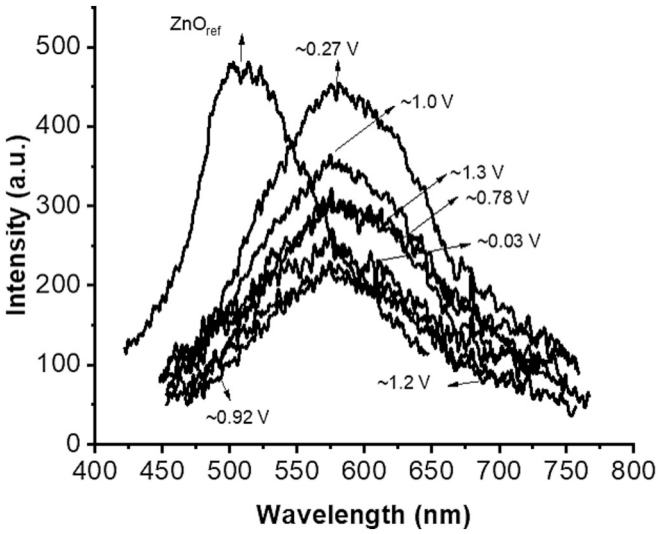

Fig. 7. Emission spectra of particles obtained from ASBA with different residual voltage [Authors].

respectively. The intense peak at 438 cm^{-1}, attributed to the E_2 (high) mode, is a signature of the wurtzite ZnO structure and indicates high crystallinity (Zheng et al., 2011). The peak at 584 cm^{-1} was attributed specifically to oxygen-related defects, consistent with previous reports on ZnO (Güell et al., 2016; Šćepanović et al., 2010; Shaik et al., 2015). Fig. 6**.** also presents the Raman spectra of particles recovered from ASAB samples with residual voltages of 1.5, 1.3, 1.2, 1.0, 0.92, 0.78, 0.27, and 0.03 V. In all samples except for the one recovered from batteries with a residual voltage of 1.5 V four vibrational modes characteristic of the wurtzite ZnO structure were identified: E_2 (low), A_1 (TO), E_1 (TO), and E_2 (high), confirming the presence of ZnO. The sample recovered from batteries with 1.5 V residual voltage, corresponding to metallic zinc, did not exhibit Raman-active vibrational modes in the 200 – 700 cm^{-1} range. This absence of ZnO-related peaks further supports the phase identification obtained through XRD and DSC analyses.

In samples recovered from ASAB with residual voltages between 1.3 and 0.92 V, Raman spectroscopy revealed clear vibrational signatures of the ZnO phase, despite the coexistence of Zn and ZnO confirmed by other techniques. These modes were located at 334, 380, 408, and 438 cm^{-1}, corresponding to E_2 (low), A_1 (TO), E_1 (TO), and E_2 (high), respectively (Xue et al., 2014; Das and Pradhan, 2010; Morozov et al., 2015). Notably, none of the spectra exhibited peaks in the 500 – 600 cm^{-1} range, suggesting a relatively low concentration of structural defects such as interstitial zinc (Zn_i) or oxygen vacancies (V_0) in ZnO formed within this voltage range.

Luminescence

Fig. 7 presents the photoluminescent emission spectra of ZnO$_{ref}$, alongside those recovered from ASAB samples with average residual voltages of 1.3, 1.2, 1.0, 0.92, 0.78, 0.27, and 0.03 V. The sample corresponding to 1.5 V, identified as metallic zinc, was excluded due to the absence of luminescent emission

The ZnO$_{ref}$ exhibited a broad emission band ranging from 420 to 640 nm, with a peak centered at 520 nm (2.38 eV). This green emission is attributed to electron recombination at singly ionized oxygen vacancies (V_0^+) (Roy and Roy, 2015; Zhao et al., 2016). In contrast, ZnO particles recovered ASBA with residual voltages between 1.3 and 0.03 V exhibited emission bands spanning 450 to 750 nm, with peak positions as follows: 590 nm (1.3 V), 578 nm (1.2 V), 585 nm (1.0 V), 587 nm (0.92 V), 589 nm (0.78 V), 587 nm (0.27 V), and 576 nm (0.03 V). These emissions fall within the yellow region of the visible spectrum and are associated with interstitial oxygen defects (O_i) in the ZnO lattice.

Interstitial oxygen alters the electronic structure of ZnO by introducing localized energy levels within the bandgap, facilitating radiative recombination processes. According to (Lotfi Orimi, 2013), two mechanisms can explain this yellow luminescence: (i) transitions from the conduction band edge to a deep acceptor level introduced by O_i, and (ii) transitions from a deep donor level to the valence band, also influenced by O_i. These transitions result in photon emissions with energies lower than the bandgap of ZnO, consistent with the observed yellow-orange luminescence. The gradual redshift in the emission peak—from 576 nm to 590 nm—as the residual voltage decreases suggests an increasing concentration or stabilization of interstitial oxygen defects during battery discharge. This trend aligns with previous reports indicating that ZnO synthesized under varying conditions exhibits yellow-orange luminescence due to O_i-related defect states (Lotfi Orimi, 2013; Kenanakis et al., 2011; Lv et al., 2019). Importantly, this luminescent behavior correlates with the morphological evolution observed in SEM analyses. The elongated microrod structures recovered at lower voltages, with higher aspect ratios and rough surfaces, likely promote defect formation and enhance radiative recombination. This morphology-defect-emission relationship underscores the potential of ZnO recovered from ASAB for optoelectronic applications, where defect engineering and shape control are critical for performance optimization

These observations underscore that ZnO obtained by thermal oxidation of metallic Zn (ZnO$_{ref}$) and ZnO recovered from spent alkaline battery anodes (ASBA) exhibit distinct defect-related luminescence behaviors. While ZnO$_{ref}$ shows green emission associated with oxygen vacancies (V_0), the recovered ZnO displays yellow emission linked to interstitial oxygen defects (O_i). This contrast reflects fundamental differences in defect chemistry and lattice disorder between synthesized reference ZnO and battery-derived ZnO, emphasizing that their optical responses are not interchangeable and must be interpreted according to their origin and processing history.

Conclusions

The performance and recyclability of alkaline batteries are strongly influenced by the electrochemical efficiency of zinc utilization, which is often limited by passivation phenomena and structural heterogeneity, thereby reducing the theoretical capacity of the cell. The Zn/ZnO ratio observed in recovered anodes serves as a key indicator of both the electrochemical discharge history and the underlying physicochemical

processes, including dissolution, precipitation, and surface passivation. A clear understanding of these mechanisms is essential for developing recycling strategies that maximize the efficiency and sustainability of zinc extraction from spent batteries. Building on this perspective, the present study provides experimental evidence that directly links the Zn/ZnO phase composition to the residual voltage of spent alkaline batteries.

The characterization of materials recovered from the anodes of spent alkaline batteries with residual voltages between 1.3 V and 0.92 V in this study, revealed the coexistence of Zn/ZnO phases, indicating incomplete oxidation of metallic zinc during battery discharge. To obtain pure ZnO, thermal post-treatment of the Zn/ZnO mixture is proposed as a viable strategy, enabling full conversion of residual Zn into ZnO. This opens promising avenues for future research focused on evaluating the physicochemical and functional properties of ZnO after controlled heat treatments.

In contrast, batteries with residual voltages below 0.78 V yielded exclusively the ZnO phase, demonstrating that deeper discharge correlates with complete oxidation. The ZnO recovered under these conditions exhibits micrometer-sized bar morphologies with voltage-dependent aspect ratios, suggesting a discharge-driven growth mechanism. XRD analysis confirmed good crystallinity, while Raman and photoluminescence studies revealed the presence of interstitial oxygen defects (O_i), responsible for yellow-orange luminescence when excited at 365 nm. This emission behavior, linked to defect-related electronic transitions, highlights the potential of this ZnO for optoelectronic and sensing applications.

Crucially, the recovery methodology employed avoids chemical reagents, minimizes toxic waste generation, and operates at significantly lower energy costs compared to conventional hydro- and pyrometallurgical processes. This makes it a sustainable and environmentally friendly alternative for ZnO production.

In summary, ZnO recovered from spent alkaline batteries not only represents a green raw material, but also exhibits properties suitable for incorporation into advanced functional materials, including polymeric composites for surface coatings, flexible electronics, medical devices, and antimicrobial systems. Its valorization contributes to circular economy efforts and offers a scalable route for waste-to-resource transformation.

CRediT authorship contribution statement

Juan Carlos Rodriguez Lopez: Writing – original draft, Methodology, Investigation. **Enrique Vigueras Santiago:** Writing – review & editing, Supervision, Resources, Funding acquisition, Formal analysis, Conceptualization. **N. García-González:** Supervision, Methodology, Formal analysis. **V.H. Castrejón-Sánchez:** Writing – original draft, Validation, Formal analysis. **Marco Camacho-López:** Writing – original draft, Validation, Formal analysis. **Susana Hernández López:** Writing – review & editing, Validation, Supervision, Project administration, Investigation, Formal analysis, Conceptualization.

Declaration of competing interest

The authors declare that they have no known competing financial interests or personal relationships that could have appeared to influence the work reported in this paper.

Acknowledgements

Special thanks are extended to the Academia-Industry Cooperation Center of the Technological Institute of Jocotitlán for granting access to advanced characterization equipment, including X-ray Diffraction (XRD), Scanning Electron Microscopy (SEM), and Raman spectroscopy, within the framework of the project titled *Development of a Prototype Filter for Water Purification from the Hap/ZnO Compound*. Juan Carlos Rodríguez López (CVU 1313982) expresses his sincere gratitude to CONAHCYT (SECIHTI) for the support received through a master's scholarship, which enabled his active participation in this study.

Funding

This study was supported by grant A1-S-33899 from SECIHTI and by grant 7217/25CIB from SIEA-UAEMEX.

Appendix A. Supplementary data

Supplementary data to this article can be found online at https://doi.org/10.1016/j.wmb.2026.100281.

References

Al-luhaibi, A.A., Sendi, R.K., 2022. Synthesis, potential of hydrogen activity, biological and chemical stability of zinc oxide nanoparticle preparation by sol–gel: a review. JRRAS 15 (3), 238–254. https://doi.org/10.1016/j.jrras.2022.07.008.

Liu, M., Nam, C.Y., Black, C.T., Kamcev, J., Zhang, L., 2013. Enhancing water splitting activity and chemical stability of zinc oxide nanowire photoanodes with ultrathin titania shells. J. Phys. Chem. C 117 (26), 13396–13402. https://doi.org/10.1021/jp404032p.

Nguyen, T., Adjeroud, N., Guennou, M., Guillot, J., Fleming, Y., Papon, A.M., Arl, D., Menguelti, K., Joly, R., Gambacorti, N., Polesel-Maris, J., 2020. Controlling electrical and optical properties of zinc oxide thin films grown by thermal atomic layer deposition with oxygen gas. Results Mater. 6, 100088. https://doi.org/10.1016/j.rinma.2020.100088.

Kumar, S.S., Venkateswarlu, P., Rao, V.R., Rao, G.N., 2013. Synthesis, characterization and optical properties of zinc oxide nanoparticles. Int. Nano Lett. 3, 30. https://doi.org/10.1186/2228-5326-3-30.

Gulab, H., Fatima, N., Tariq, U., Gohar, O., Irshad, M., Khan, M.Z., Saleem, M., Ghaffar, A., Hussain, M., Jan, A.K., Humayun, M., Motola, M., Hanif, M.B., 2024. Advancements in zinc oxide nanomaterials: synthesis, properties, and diverse applications. Nano-Struct. Nano-Objects 39, 101271. https://doi.org/10.1016/j.nanoso.2024.101271.

Noman, M.T., Amor, N., Petru, M., 2022. Synthesis and applications of ZnO nanostructures (ZONSs): a review. Crit. Rev. Solid State Mater. Sci. 47 (2), 99–141. https://doi.org/10.1080/10408436.2021.1886041.

Cebriano, T., García-Díaz, I., López Fernández, A., Fernández, P., López, F.A., 2017. Synthesis and characterization of ZnO micro- and nanostructures grown from recovered ZnO from spent alkaline batteries. J. Environ. Chem. Eng. 5 (3), 2903–2911. https://doi.org/10.1016/j.jece.2017.05.052.

Deep, A., Kumar, K., Kumar, P., Kumar, P., Sharma, A.L., Gupta, B., Bharadwaj, L.M., 2011. Recovery of pure ZnO nanoparticles from spent Zn-MnO2 alkaline batteries. Environ. Sci. Technol. 45 (24), 10551–10556. https://doi.org/10.1021/es201744t.

Lopez, G.P., Gallegos, M.V., Peluso, M.A., Damonte, L.C., Sambeth, J.E., Bellotti, N., 2023. ZnO recovered from spent alkaline batteries as antimicrobial additive for waterborne paints. Emerg. Mater. 6, 147–158. https://doi.org/10.1007/s42247-022-00443-2.

Lorero, I., Campo, M., Arribas, C., Prolongo, M.G., López, F.A., Prolongo, S.G., 2022. Epoxy composites reinforced with ZnO from waste alkaline batteries. Materials 15 (8), 2842. https://doi.org/10.3390/ma15082842.

Milenio®. (2023, January 8). En México, se desechan cada año 780 millones de pilas no recargables. https://www.milenio.com/negocios/mexico-desechan-ano-780-millones-pilasrecargables#:~:text=En%20M%C3%A9xico%2C%20cada%20habitante%20consume,a%20d%C3%B3nde%20van%20a%20parar%3F.

Global Market Insights. (2024). Alkaline battery market size, share & trends analysis report. Retrieved from https://www.gminsights.com/industry-analysis/alkaline-battery-market.

Toro, L., Moscardini, E., Baldassari, L., Forte, F., Falcone, I., Coletta, J., Toro, L., 2023. A systematic review of battery recycling technologies: advances, challenges, and future prospects. Energies. 16 (18), 6571. https://doi.org/10.3390/en16186571.

Bae, S.U., Park, J.H., Park, K.T., Shin, J.H., 2025. Pyrometallurgical eco-recycling for Zn and MnO recovery from spent alkaline and Zn–C batteries. J. Mater. Cycles Waste Manag. 27, 572–583. https://doi.org/10.1007/s10163-024-02123-1.

Jain, M., Kumar, D., Chaudhary, J., Kumar, S., Sharma, S., Verma, A.S., 2023. Review on e-waste management and its impact on the environment and society. Waste Manag. Bull. 1 (3), 34–44. https://doi.org/10.1016/j.wmb.2023.06.004.

Mandeep, M., Vishal, V., Antil, N., Malik, J., Monika, 2019. Recovery of ZnO nanoparticles from spent Zn–C batteries and their application in the degradation of methyl orange dye. Int. J. Adv. Acad. Stud. 1 (1), 213–218.

Stefan, M., Kocabas, B., Güngör, A., Toloman, D., Rostas, A.M., Suciu, R.C., Macavei, S., Ganea, I., Perhaita, I., Tripon, S., Leostean, C., Erdem, E., Popa, A., 2024. Manganese-doped zinc oxide recycled from spent alkaline batteries for photocatalysis and supercapacitor applications. J Energy Storage. 99 (B), 113419. https://doi.org/10.1016/j.est.2024.113419.

Sunaina, S., Sreekanth, M., Manolata Devi, M., Sethi, V., Ghosh, S., Mehta, S.K., Ganguli, A.K., Jha, M., 2021. New approach for fabrication of vertically oriented ZnO-based field emitter derived from waste primary batteries. Mater. Sci. Eng.: B. 274, 115480. https://doi.org/10.1016/j.mseb.2021.115480.

REDWAY, (2024, October 3). The Decline in Voltage of Alkaline Batteries: A Comprehensive Analysis of Impact on Device Performance. https://www.redwaybattery.com/es/tag/aa/.

Collins, J., Gourdin, G., Qu, D., 2018. Modern applications of green chemistry: renewable energy, in: B. Török, T. Dransfield (Eds.), Green Chemistry, Elsevier, pp. 771–860. Doi: 10.1016/B978-0-12-809270-5.00028-5.

Horna, Q.C., Shao-Horn, Y., 2003. Morphology and spatial distribution of ZnO formed in discharged alkaline Zn–MnO_2 AA cells. J. Electrochem. Soc. 150 (5), A652–A658. https://doi.org/10.1149/1.1566014.

Durena, R., Zukuls, A., 2023. A short review: comparison of zinc–manganese dioxide batteries with different pH aqueous electrolytes. Batteries. 9, 311. https://doi.org/10.3390/batteries9060311.

Bantikatla, H., Kumar, K., Thodeti, S., Bantikatla, H.B., Kumar, Y.K., Sathish, B., 2019. Synthesis and characterization of ZnO nanostructures by oxidation technique. IJARSE 6 (11), 539–544. https://www.researchgate.net/publication/336891878.

Noohi, Z., Nosouhian, S., Niroumand, B., Timelli, G., 2022. Use of low melting point metals and alloys (Tm < 420 °C) as phase change materials: a review. Metals 12 (6), 945. https://doi.org/10.3390/met12060945.

Kahouli, M., Barhoumi, A., Bouzid, A., Al-Hajry, A., Guermazi, S., 2015. Structural and optical properties of ZnO nanoparticles prepared by direct precipitation method. Superlattices Microstruct. 85, 7–23. https://doi.org/10.1016/j.spmi.2015.05.007.

Raoufi, D., 2013a. Synthesis and microstructural properties of ZnO nanoparticles prepared by precipitation method. Renew. Energy 50, 932–937. https://doi.org/10.1016/j.renene.2012.08.076.

Dhingra, M., Gupta, R., Annapoorni, S., 2018. Defect induced ferromagnetism in Zn/ZnO interfaces. Cryst. Res. Technol. 53, 1700293. https://doi.org/10.1002/crat.201700293.

de Sousa e Silva, R.L., Franco Jr., A., 2020. Raman spectroscopy study of structural disorder degree of ZnO ceramics. Mater. Sci. Semicond. Process. 119, 105227. https://doi.org/10.1016/j.mssp.2020.105227.

Xue, X., Wang, T., Jiang, X., Jiang, J., Pan, C., Wu, Y., 2014. Interaction of hydrogen with defects in ZnO nanoparticles-studied by positron annihilation, Raman and photoluminescence spectroscopy. Cryst. Eng. Comm. 16 (6), 1207–1216. https://doi.org/10.1039/c3ce42202j.

Zheng, J.H., Jiang, Q., Lian, J.S., 2011. Synthesis and optical properties of flower-like ZnO nanorods by thermal evaporation method. Appl. Surf. Sci. 257 (11), 5083–5087. https://doi.org/10.1016/j.apsusc.2011.01.025.

Güell, F., Martínez-Alanis, P.R., Khachadorian, S., Rubio-García, J., Franke, A., Hoffmann, A., Santana, G., 2016. Raman and photoluminescence properties of ZnO nanowires grown by a catalyst-free vapor-transport process using ZnO nanoparticle seeds. Phys. Status Solidi B. 253 (5), 883–888. https://doi.org/10.1002/pssb.201552651.

Šćepanović, M., Grujić-Brojčin, M., Vojisavljević, K., Bernikc, S., Srećković, T., 2010. Raman study of structural disorder in ZnO nanopowders. J. Raman Spectrosc. 41 (9), 914–921. https://doi.org/10.1002/jrs.2546.

Shaik, U.P., Kumar, P.A., Krishna, M.G., Rao, S.V., 2015. Morphological manipulation of the nonlinear optical response of ZnO thin films grown by thermal evaporation. Mater. Res. Express 1 (4), 046201. https://doi.org/10.1088/2053-1591/1/4/046201.

Das, J., Pradhan, S.K., Sahu, D.R., Mishra, D.K., Sarangi, S.N., Nayak, B.B., Verma, S., Roul, B.K., 2010. Micro-Raman and XPS studies of pure ZnO ceramics, Phys. B: Condens. Matter, 405(10), 2492–2497. Doi: 10.1016/j.physb.2010.03.020.

Morozov, I.G., Belousova, O.V., Ortega, D., Mafina, M.K., Kuznetcov, M.V., 2015. Structural, optical, XPS and magnetic properties of Zn particles capped by ZnO nanoparticles. J. Alloys Compd. 633, 237–245. https://doi.org/10.1016/j.jallcom.2015.01.285.

Roy, N., Roy, A., 2015. Growth and temperature dependent photoluminescence characteristics of ZnO tetrapods. Ceram. Int. 41 (3), 4154–4160. https://doi.org/10.1016/j.ceramint.2014.11.113.

Zhao, J.H., Liu, C.J., Lv, Z.H., 2016. Photoluminescence of ZnO nanoparticles and nanorods. Optik 127 (3), 1421–1423. https://doi.org/10.1016/j.ijleo.2015.11.018.

Lotfi Orimi, R., 2013. Investigation of the effect of annealing on the photoluminescence properties of ZnO nanoparticles, synthesized at low temperature. Opt. Mater. 35(3), 657–660. Doi: 10.1016/j.optmat.2012.10.047.

Kenanakis, G., Androulidaki, M., Vernardou, D., Katsarakis, N., Koudoumas, E., 2011. Photoluminescence study of ZnO structures grown by aqueous chemical growth. Thin Solid Films 520 (4), 1353–1357. https://doi.org/10.1016/j.tsf.2011.04.123.

Lv, J., Li, C., Chai, Z., 2019. Defect luminescence and its mediated physical properties in ZnO. J. Lumin. 208, 225–237. https://doi.org/10.1016/j.jlumin.2018.12.050.